Supplement to The Berkeley High Resolution Tropospheric NO$_2$ Product

Joshua L. Laughner, Qindan Zhu, and Ronald. C. Cohen

S1   WRF-Chem Model

For years 2005–2006, the chemical initial and boundary conditions for WRF-Chem are taken from the GEOS-Chem v9-02 model with the following changes to the chemistry:

- The rate of the reaction NO$_2$ + OH $\longrightarrow$ HNO$_3$ is changed from that recommended in Sander et al. (2011) to that in Henderson et al. (2012).

- The rates of the formation and dissociation of HNO$_4$ are changed from that recommended in Sander et al. (2011) to that in Bacak et al. (2011).

- The rate of hydrolysis of N$_2$O$_5$ to HNO$_3$ was reduced to 10% of the value from Evans and Jacob (2005), as recommended in Brown et al. (2009).

- The number of moles of NO emitted per lightning flash was increased by 33% to 665 mol NO flash^{-1} (midlatitudes) and 346 mol NO flash^{-1} (tropics) based on the findings of Nault et al. (2017)

To provide output for WRF-Chem boundary conditions from 2005–2006, the GEOS-Chem model is spun up for the calendar year 2004.

S2   Difference in average VCDs due to profile temporal resolution

The difference in the NO$_2$ VCDs when using daily vs. monthly profiles must ultimately be due to differences in the AMFs. Consider an average AMF for a given location defined by:

$$\overline{A} = \frac{1}{n} \sum_{i=1}^{n} \frac{\int_{p_{s_i}}^{p_t} w_i(p) g_i(p) \, dp}{\int_{p_{s_i}}^{p_t} g_i(p) \, dp} \tag{S1}$$
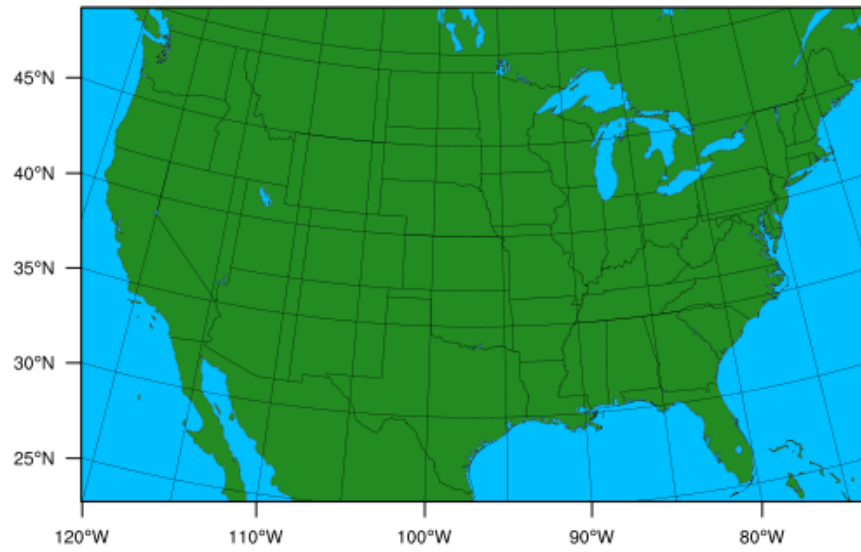
Figure S1: The WRF-Chem model domain.
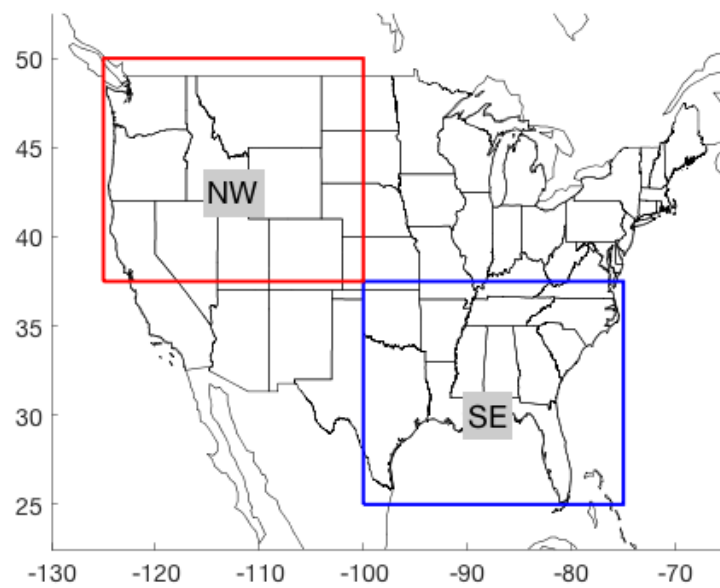
Figure S2: Regions used in testing the differences between using monthly and daily a priori NO$_2$ profiles.
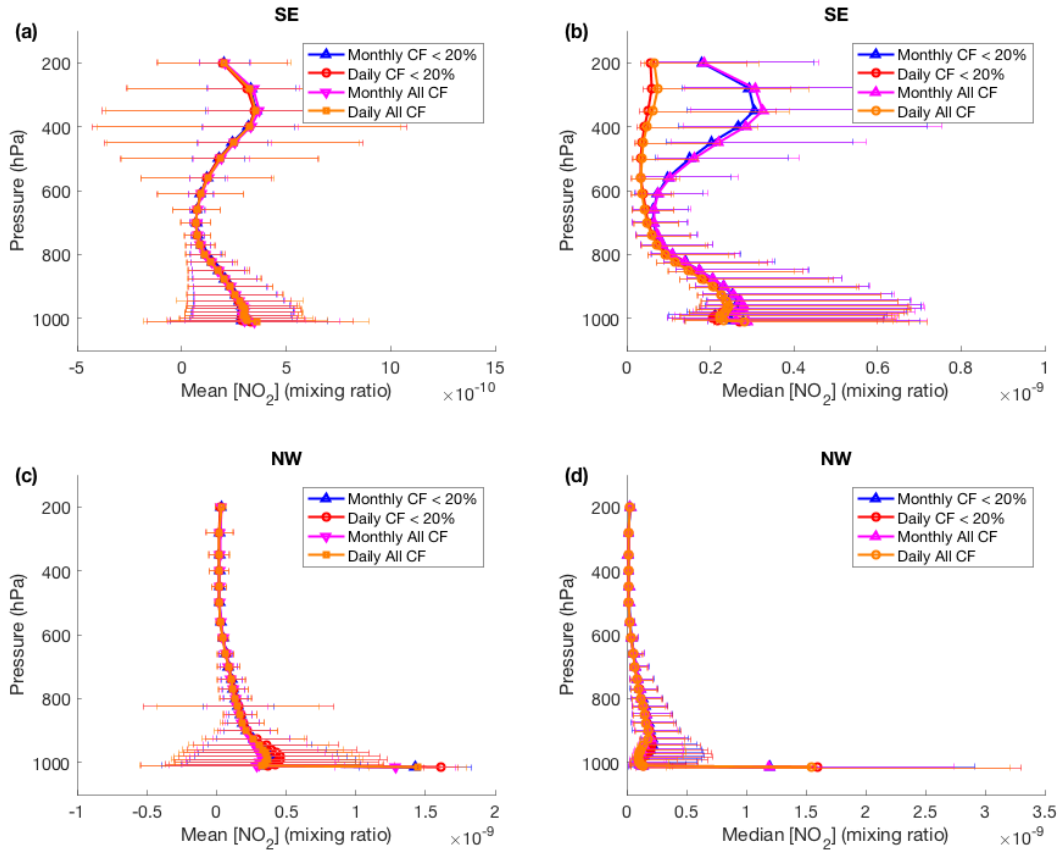
Figure S3: Mean (a,c) and median (b,d) NO$_2$ a priori profiles for the regions defined in S2 (southeast, a–b; northwest, c–d). Error bars for means are 1σ standard deviation, medians are the 25th and 75th percentiles. As in the main paper, the blue and red lines only include pixels with cloud fraction $< 20\%$, while the magenta and orange lines include all pixels.

For a given location, the surface pressure and (over the course of a month) surface reflectivity will be fairly constant, and additionally let us assume that the sun-satellite geometry will average in such a way that the scattering weights, w_i can be taken as an average, $\overline{w}$. With this assumption and assuming that $p_{s_i} = p_s$ for all i:

$$\overline{A} = \frac{1}{n} \sum_{i=1}^{n} \frac{\int_{p_s}^{p_t} \overline{w}(p) g_i(p) \, dp}{\int_{p_i}^{p_t} g_i(p) \, dp} \tag{S2}$$

$$= \int_{p_s}^{p_t} \overline{w}(p) \frac{1}{n} \sum_{i=1}^{n} S_i(p) \, dp \tag{S3}$$

where

$$S_i(p) = \frac{g_i(p)}{\int_{p_i}^{p_t} g_i(p) \, dp} \tag{S4}$$

i.e. $S_i(p)$ is the shape factor.

For the monthly average profiles, $g(p)$ is averaged temporally. Within each day, individual hours are weighted by their proximity to OMI overpass; the resulting daily average profiles are given equal weight in the monthly average:

$$\overline{g}(p) = \frac{1}{n} \sum_{i=1}^{n} g_i(p) \tag{S5}$$

where $g_i(p)$ represents one day's profile. Therefore, the monthly average shape factor is

$$\overline{S}_M(p) = \frac{1}{n} \sum_{i=1}^{n} \frac{\overline{g}(p)}{\int_{p_s}^{p_t} \overline{g}(p) \, dp} \tag{S6}$$

$$= \frac{\overline{g}(p)}{\int_{p_s}^{p_t} \overline{g}(p) \, dp} \tag{S7}$$

$$= \frac{\frac{1}{n} \sum_{i=1}^{n} g_i(p)}{\int_{p_s}^{p_t} \frac{1}{n} \sum_{i=1}^{n} g_i(p) \, dp} \tag{S8}$$

In contrast, the average shape factor using daily profiles would be:

$$\overline{S}_D(p) = \frac{1}{n} \sum_{i=1}^{n} \frac{g_i(p)}{\int_{p_s}^{p_t} g_i(p) \, dp} \tag{S9}$$

Eq. (S8) and (S9) are not mathematically equivalent. From Figs. S3 and 6, we can infer that the daily variation in surface NO_2 does not significantly affect the average AMF, which is consistent with Laughner et al. (2016), where implementing daily profiles led to small changes in the average over most of the domain. In Eq. (S9), profiles influenced by lightning will have a larger denominator than those not influenced, and so the increase in UT NO_2 is offset by the increase in total VCD. This causes the shift towards more surface influence in the average daily shape factors in Fig. 6c. Alternately, the denominator of Eq. (S9) can be viewed as a weighting factor that is inherently smaller for lightning-influenced profiles; thus, such profiles have less influence in the shape factor.

S3 Additional figures
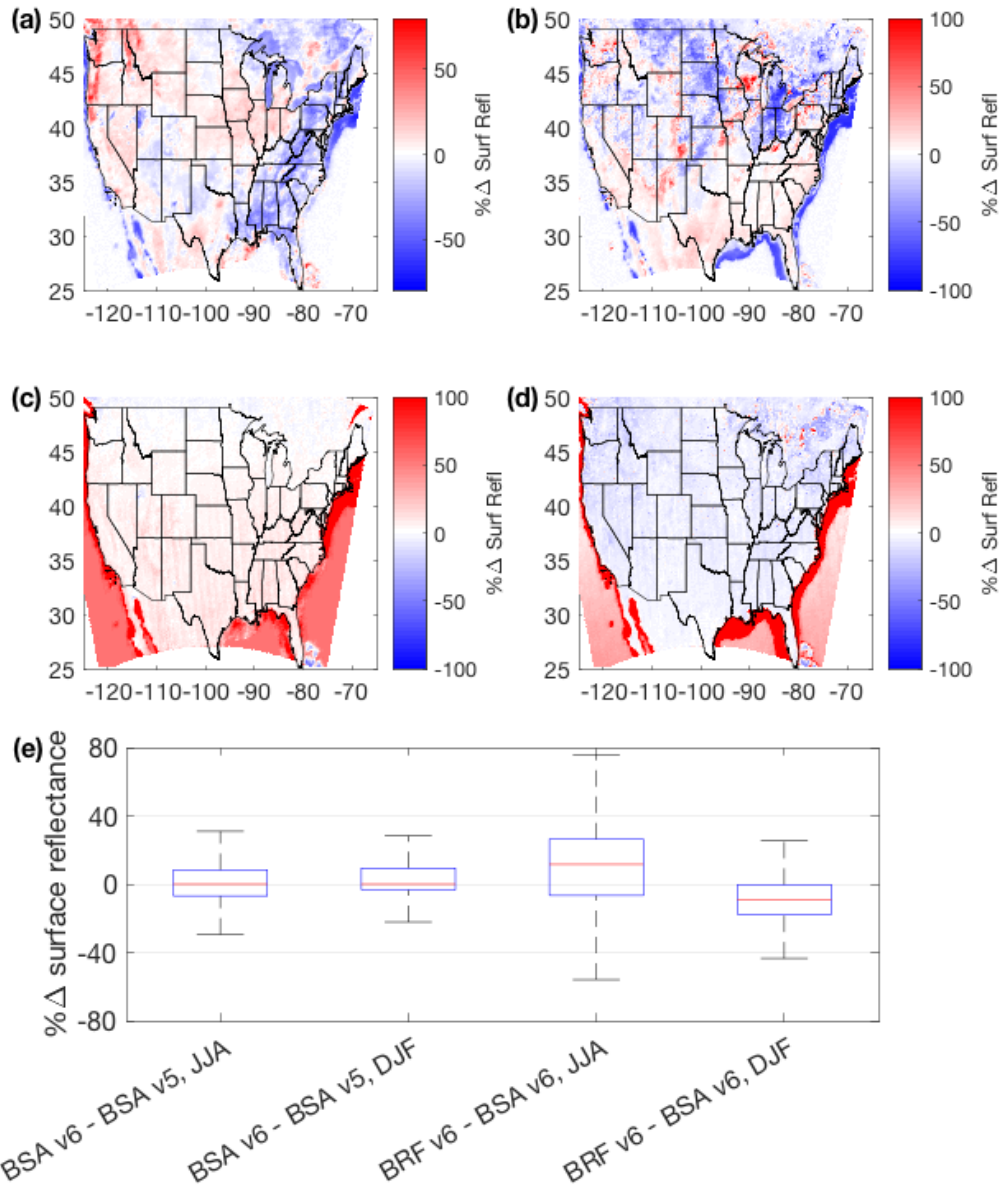
Figure S4: Attribution of changes in surface reflectance to the version 5 to version 6 MODIS product upgrade vs. the black sky to BRF upgrade. **(a,b)** Percent difference in surface reflectance using version 6 – version 5 of the MODIS black-sky albedo product (MCD43C3). **(c,d)** Percent difference in surface reflectance using a BRF – black sky, both version 6. **(a,c)** differences averaged over Jun, Jul, and Aug 2012; **(b,d)** averaged over Jan, Feb, and Dec 2012. **(e)** Box plots of percent difference in individual pixels' surface reflectances for pixels classified as land pixels, illustrating that although the average change between a black sky and BRF surface reflectance is fairly consistent, individual pixels do have significant changes, as one would expect with a geometry dependent surface reflectance. The red line marks the median, the blue box the upper and lower quartiles, and the black lines the largest and smallest non-outlier values. Outliers are omitted.
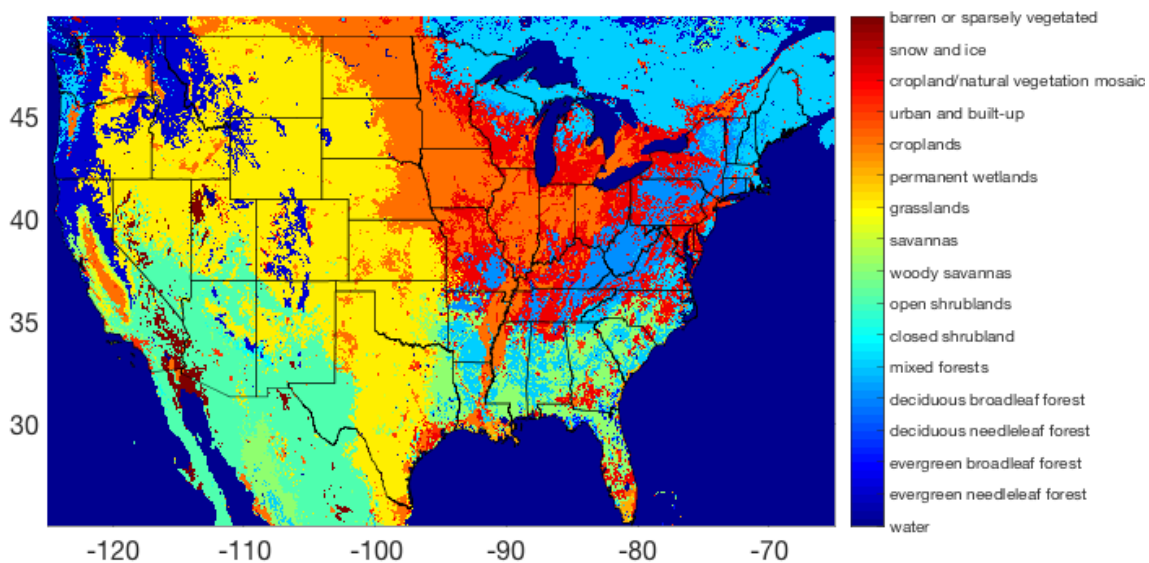
Figure S5: IGBP land cover classifications for 2012 from the MODIS MCD12C1 product
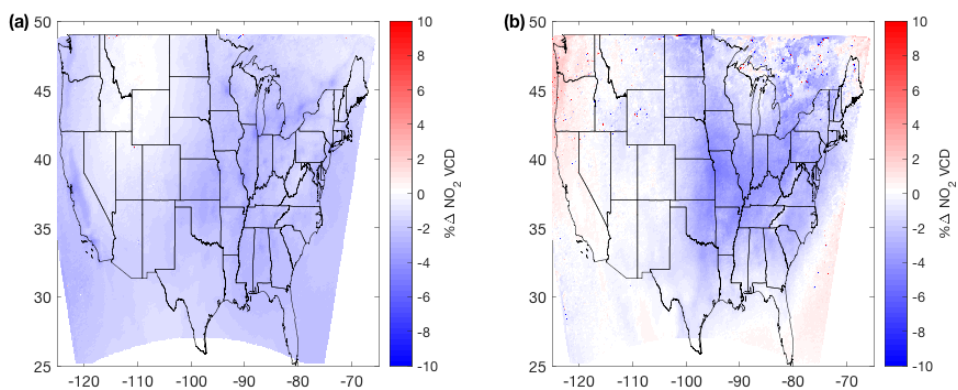
Figure S6: The percent change in total tropospheric VCDs after fixing the temperature lookup error (a) in summer (Jun–Aug) and (b) in winter (Jan, Feb, Dec).
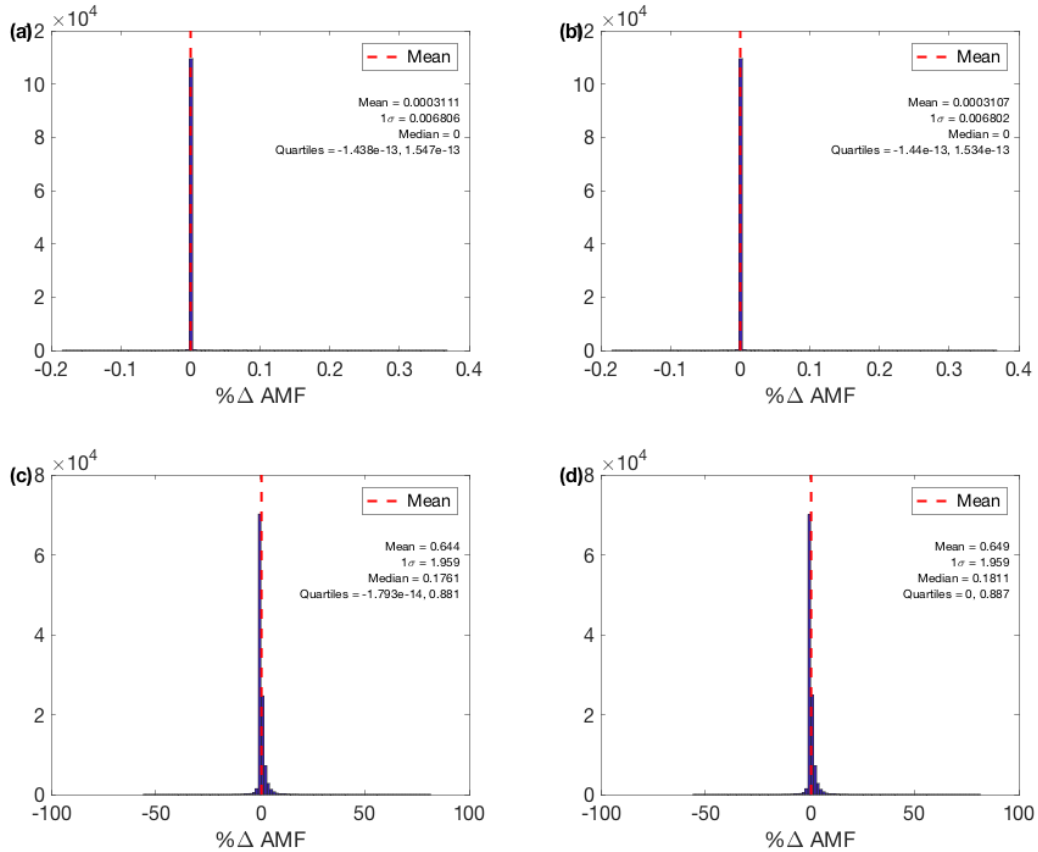
Figure S7: Percent differences between BEHR AMFs and AMFs recalculated with the published scattering weights and NO_2 a priori profiles. **(a, b)** use separate published clear and cloudy scattering weights, **(c, d)** use the v3.0A and previous cloud radiance fraction weighted average scattering weights. **(a)** and **(c)** are for total tropospheric AMFs, **(b)** and **(d)** are for visible-only AMFs.

S4 More detail on each incremental change
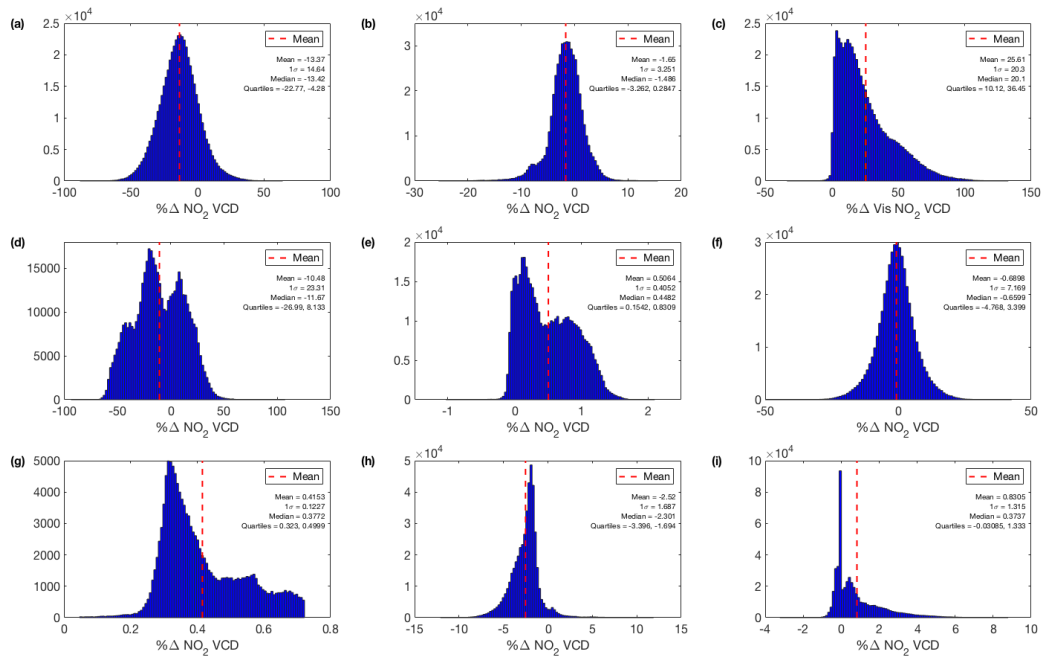
Figure S8: Histograms of the changes in JJA VCDs from Fig. 1. As in Fig. 1: **(a)** Change due to new NASA SCDs. **(b)** Change due to updated surface reflectance. **(c)** Change in visible-only VCD due to new visible-only AMF formulation. **(d)** Change due to new monthly profiles. **(e)** Changes due to new temperature profile. **(f)** Changes due to new gridding method. **(g)** Changes due to the ocean reflectance changed to 460 nm. **(h)** Change due to implementation of the variable tropopause height. **(i)** Changes due to the Zhou et al. (2009) surface pressure formulation. All averages exclude outliers, the row anomaly, and use only cloud fraction ≤ 0.2. In **(g)**, only ocean grid cells are considered.
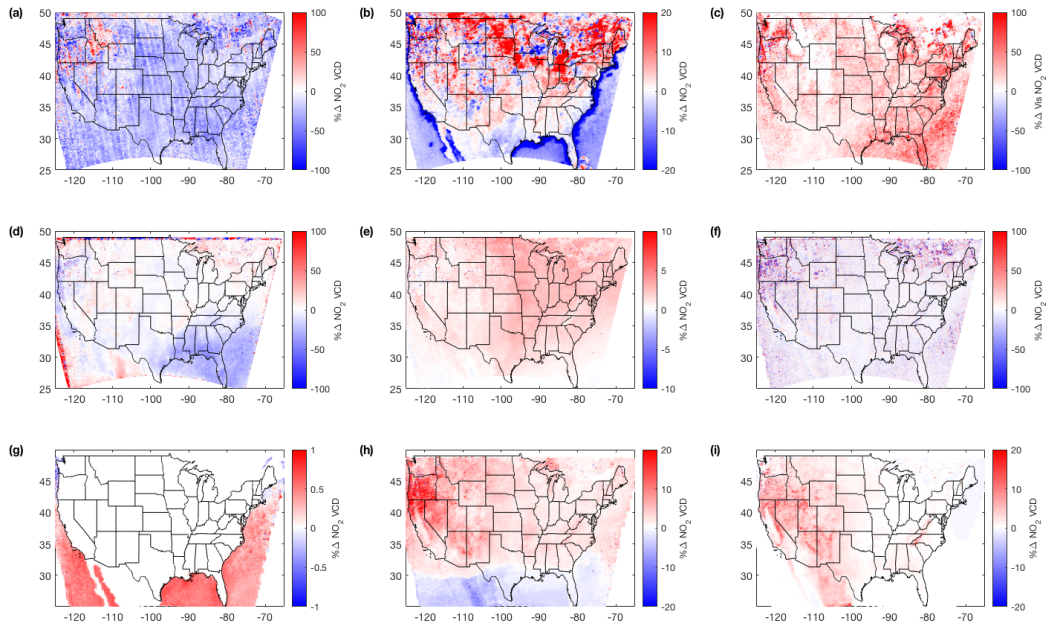
Figure S9: As Fig. 1 but for Jan, Feb, Dec 2012: changes in total tropospheric or visible-only VCDs due to individual changes. **(a)** Change due to new NASA SCDs. **(b)** Change due to updated surface reflectance. **(c)** Change in visible-only VCD due to new visible-only AMF formulation. **(d)** Change due to new monthly profiles. **(e)** Changes due to new temperature profile. **(f)** Changes due to new gridding method. **(g)** Changes due to the ocean reflectance changed to 460 nm. **(h)** Change due to implementation of the variable tropopause height. **(i)** Changes due to the Zhou et al. (2009) surface pressure formulation. All averages exclude the row anomaly and use only cloud fraction ≤ 0.2.
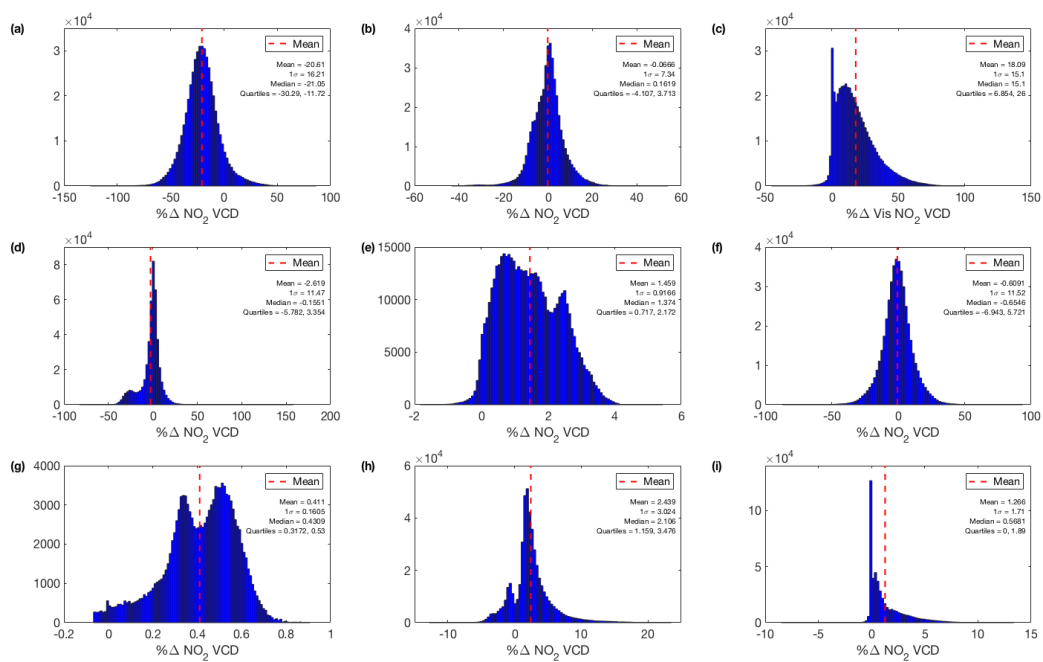
Figure S10: Histograms of the changes in DJF VCDs from Fig. S9, with outliers removed. In **(g)**, only ocean grid cells are considered.
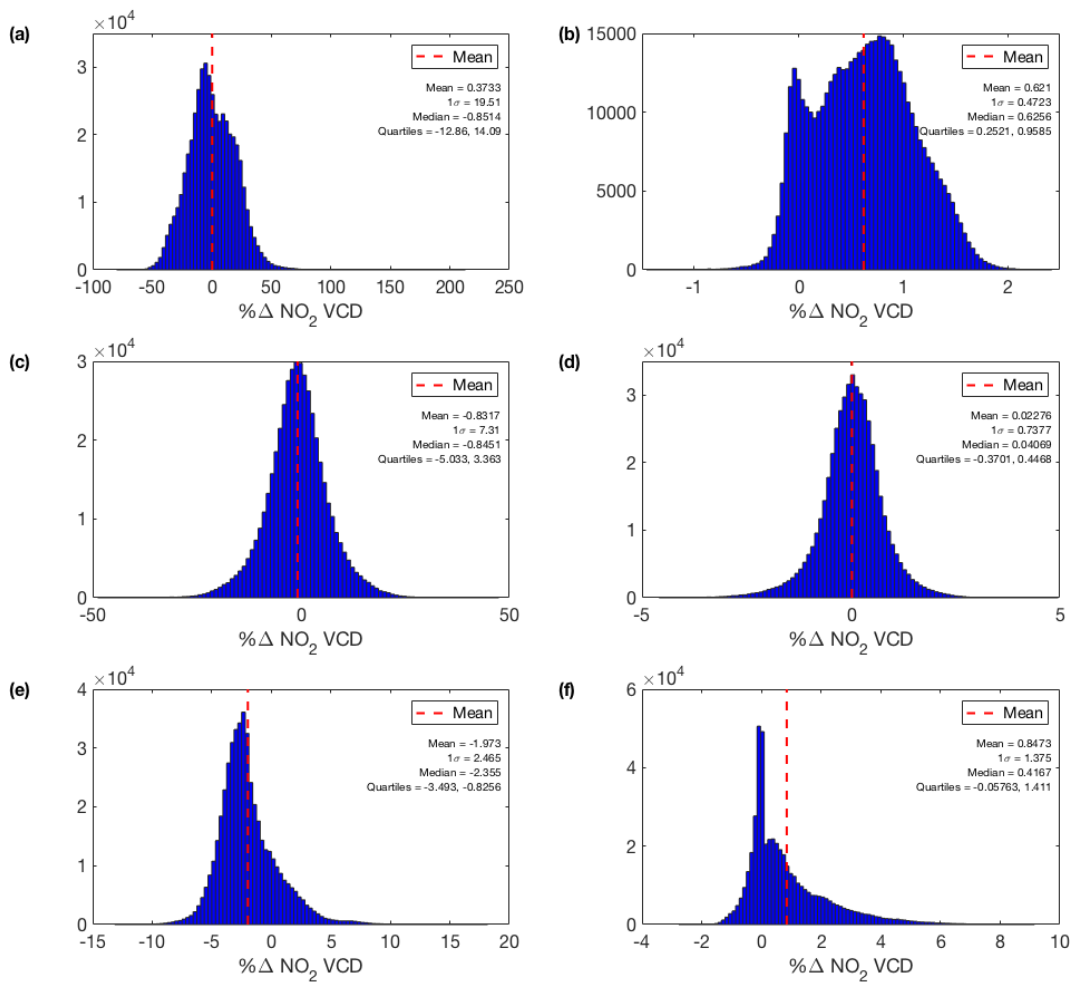
Figure S11: Histograms of the differences shown in Fig. 4.
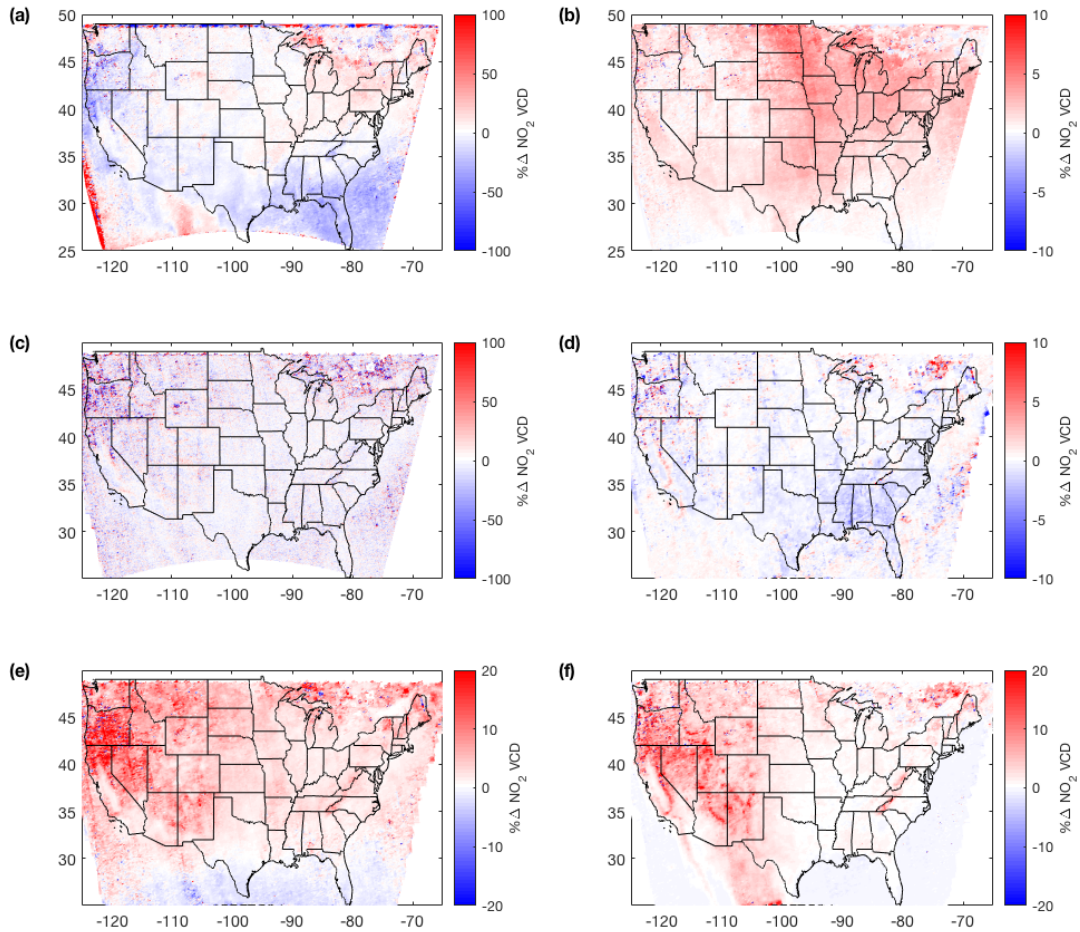
Figure S12: Similar to Fig. 4, but for DJF. Changes in the average VCDs in the subproduct using daily profiles due to: **(a)** implementation of new profiles, **(b)** new temperature profiles, **(c)** new gridding method, **(d)** change to temporal matching of daily profiles with OMI overpass and changing the ocean reflectance LUT to 460 nm, **(e)** implementing the variable tropopause height, and **(f)** the Zhou et al. (2009) surface pressure formulation. All averages exclude the row anomaly only use cloud fraction ≤ 0.2.
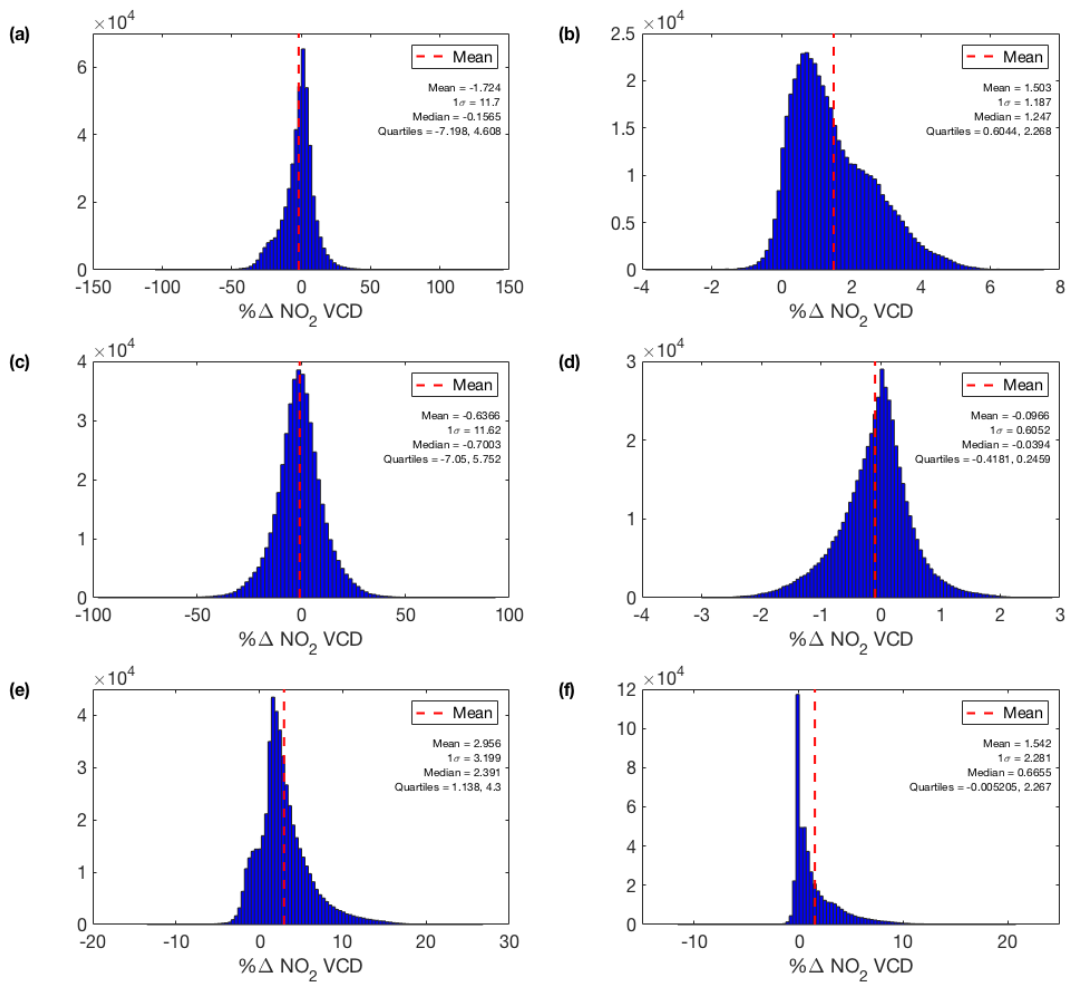
Figure S13: Histogram of the differences in Fig. S12, with outliers removed.
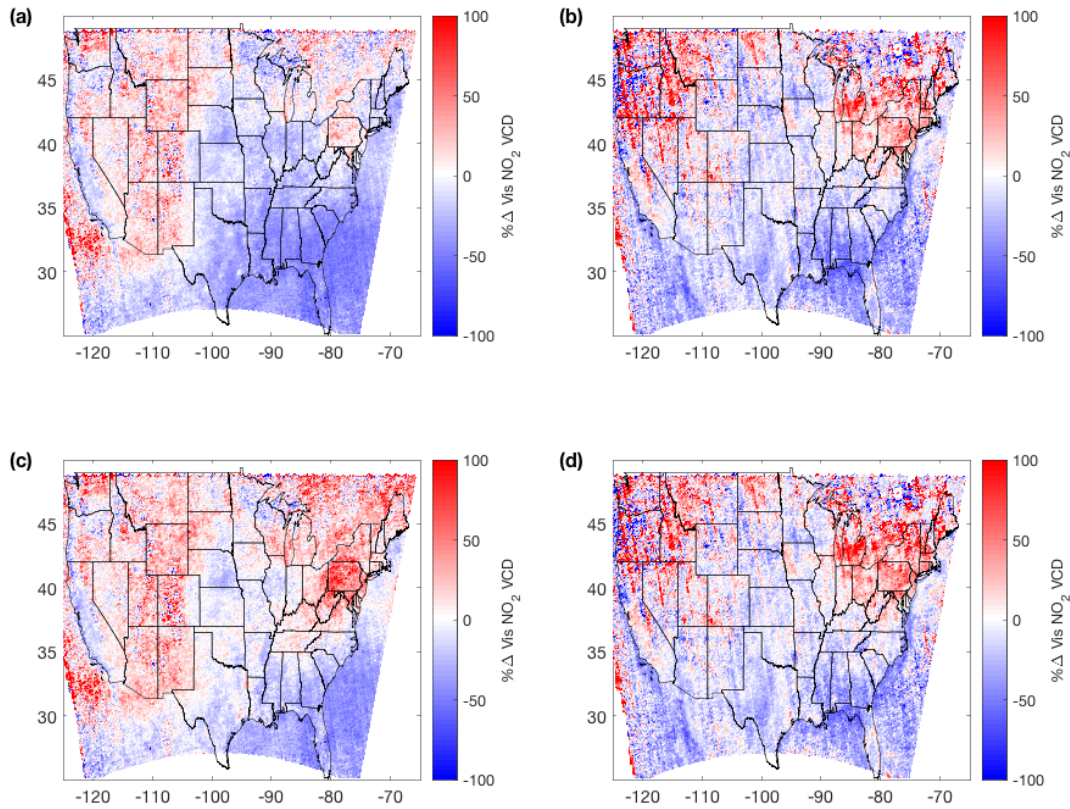
Figure S14: As Fig. 7 but for the visible-only VCDs: differences between v2.1C and v3.0B **(a,b)** v3.0B uses monthly profiles. **(c,d)** v3.0B uses daily profiles. **(a,c)** average over Jun–Aug 2012. **(b,d)** average over Jan, Feb, Dec 2012. All averages exclude the row anomaly and use only cloud fraction ≤ 0.2.

References

Bacak, A., Cooke, M., Bardwell, M., McGillen, M., Archibald, A., Huey, L., Tanner, D., Utembe, S., Jenkin, M., Derwent, R., Shallcross, D., and Percival, C.: Kinetics of the $HO_2 + NO_2$ Reaction: On the impact of new gas-phase kinetic data for the formation of HO_2NO_2 on HO_x, NO_x and HO_2NO_2 levels in the troposphere, Atmos. Environ., 45, 6414–6422, doi: 10.1016/j.atmosenv.2011.08.008, URL https://doi.org/10.1016/j.atmosenv.2011.08.008, 2011.

Brown, S. S., Dubé, W. P., Fuchs, H., Ryerson, T. B., Wollny, A. G., Brock, C. A., Bahreini, R., Middlebrook, A. M., Neuman, J. A., Atlas, E., Roberts, J. M., Osthoff, H. D., Trainer, M., Fehsenfeld, F. C., and Ravishankara, A. R.: Reactive uptake coefficients for N2O5determined from aircraft measurements during the Second Texas Air Quality Study: Comparison to current model parameterizations, J. Geophys. Res., 114, doi: 10.1029/2008jd011679, URL https://doi.org/10.1029/2008jd011679, 2009.

Evans, M. J. and Jacob, D. J.: Impact of new laboratory studies of N2O5hydrolysis on global model budgets of tropospheric nitrogen oxides, ozone, and OH, Geophys. Res. Lett., 32, doi: 10.1029/2005gl022469, URL https://doi.org/10.1029/2005gl022469, 2005.

Henderson, B. H., Pinder, R. W., Crooks, J., Cohen, R. C., Carlton, A. G., Pye, H. O. T., and Vizuete, W.: Combining Bayesian methods and aircraft observations to constrain the $HO^. + NO_2$ reaction rate, Atmospheric Chemistry and Physics, 12, 653–667, doi: 10.5194/acp-12-653-2012, URL https://www.atmos-chem-phys.net/12/653/2012/, 2012.

Laughner, J. L., Zare, A., and Cohen, R. C.: Effects of daily meteorology on the interpretation of space-based remote sensing of NO_2, Atmospheric Chemistry and Physics, 16, 15 247–15 264, doi: 10.5194/acp-16-15247-2016, URL http://www.atmos-chem-phys.net/16/15247/2016/, 2016.

Nault, B. A., Laughner, J. L., Wooldridge, P. J., Crounse, J. D., Dibb, J., Diskin, G., Peischl, J., Podolske, J. R., Pollack, I. B., Ryerson, T. B., Scheuer, E., Wennberg, P. O., and Cohen, R. C.: Lightning NO_x Emissions: Reconciling Measured and Modeled Estimates With Updated NO_x Chemistry, Geophys. Res. Lett., doi: 10.1002/2017GL074436, 2017.

Sander, S. P., Friedl, R. R., Abbatt, J. P. D., Barker, J. R., Burkholder, J. B., Golden, D. M., Kolb, C. E., Kurylo, M. J., Moortgat, G. K., Wine, P. H., Huie, R. E., and Orkin, V. L.: Chemical Kinetics and Photochemical Data for Use in Atmospheric Studies: Evaluation Number 17, Tech. rep., Jet Propulsion Laboratory, 2011.

Zhou, Y., Brunner, D., Boersma, K. F., Dirksen, R., and Wang, P.: An improved tropospheric NO_2 retrieval for OMI observations in the vicinity of mountainous terrain, Atmos. Meas. Tech., 2, 401–416, doi: 10.5194/amt-2-401-2009, URL https://www.atmos-meas-tech.net/2/401/2009/, 2009.